



Gravity waves generated by the Hunga Tonga-Hunga Ha'apai volcanic eruption and their global propagation in the mesosphere/lower thermosphere observed by meteor radars and modeled with the High-Altitude General Mechanistic Circulation Model

Gunter Stober¹, Sharon L. Vadas², Erich Becker², Alan Liu³, Alexander Kozlovsky⁴, Diego Janches⁵, Zishun Qiao³, Witali Krochin¹, Guochun Shi¹, Wen Yi⁶, Jie Zeng^{6,1}, Peter Brown^{7,8}, Denis Vida⁷, Neil Hindley²⁴, Christoph Jacobi⁹, Damian Murphy¹⁰, Ricardo Buriti¹¹, Vania Andrioli^{12,13}, Paulo Batista¹², John Marino¹⁴, Scott Palo¹⁴, Denise Thorsen¹⁵, Masaki Tsutsumi^{16,17}, Njål Gulbrandsen¹⁸, Satonori Nozawa¹⁹, Mark Lester²⁰, Kathrin Baumgarten²¹, Johan Kero²², Evgenia Belova²², Nicholas Mitchell^{23,24}, and Na Li²⁵

¹Institute of Applied Physics & Oeschger Center for Climate Change Research, Microwave Physics, University of Bern, Bern, Switzerland

²North West Research Associates (NWRA), Boulder, Colorado, USA

³Center for Space and Atmospheric Research and Department of Physical Sciences, Embry-Riddle Aeronautical University, Daytona Beach, Florida, USA

⁴Sodankylä Geophysical Observatory, University of Oulu, Finland

⁵ITM Physics Laboratory, NASA Goddard Space Flight Center, Greenbelt, MD, USA

⁶CAS Key Laboratory of Geospace Environment/CAS Center for Excellence in Comparative Planetology, Anhui Mengcheng Geophysics National Observation and Research Station, University of Science and Technology of China, Hefei, China

⁷Dept. of Physics and Astronomy, University of Western Ontario, London, Ontario, Canada

⁸Western Institute for Earth and Space Exploration, University of Western Ontario, London, Ontario, Canada

⁹Institute for Meteorology, Leipzig University, Leipzig, Germany

¹⁰Australian Antarctic Division, Kingston, Tasmania, Australia

¹¹Department of Physics, Federal University of Campina Grande, Campina Grande, Brazil

¹²National Institute for Space Research (INPE), São José dos Campos, Brazil

¹³China-Brazil Joint Laboratory for Space Weather, NSSC/INPE, São José dos Campos, Brazil

¹⁴Colorado Center for Astrodynamics Research, University of Colorado Boulder, Boulder, CO, USA

¹⁵University of Alaska, Fairbanks, USA

¹⁶National Institute of Polar Research, Tachikawa, Japan

¹⁷The Graduate University for Advanced Studies (SOKENDAI), Tokyo, Japan

¹⁸Tromsø Geophysical Observatory, UiT - The Arctic University of Norway, Tromsø, Norway

¹⁹Institute for Space-Earth Environmental Research, Nagoya University, Japan

²⁰University of Leicester, Leicester, UK

²¹Fraunhofer Institute for Ceramic Technologies and Systems IKTS, Smart Ocean Technologies, Rostock, Germany

²²Swedish Institute of Space Physics (IRF), Kiruna, Sweden

²³British Antarctic Survey, Cambridge, CB3 0ET, UK

²⁴Department of Electronic and Electrical Engineering, University of Bath, Bath, UK

²⁵National Key Laboratory of Electromagnetic Environment, China Research Institute of Radiowave Propagation, Qingdao, China



Correspondence: gunter.stober@unibe.ch

Abstract. The Hunga Tonga-Hunga Ha‘apai volcano erupted on 15th January 2022, launching Lamb waves and gravity waves into the atmosphere. In this study, we present results using 13 globally distributed meteor radars and identify the volcanic-caused gravity waves in the mesospheric/lower thermospheric winds. Leveraging the High-Altitude Mechanistic General Circulation Model (HIAMCM), we compare the global propagation of these gravity waves. We observed an eastward propagating gravity wave packet with an observed phase speed of 240 ± 5.7 m/s and a westward propagating gravity wave with an observed phase speed of 166.5 ± 6.4 m/s. We identified these waves in the HIAMCM and obtained very good agreement of the observed phase speeds of 239.5 ± 4.3 m/s and 162.2 ± 6.1 m/s for the eastward and the westward waves, respectively. Considering that HIAMCM perturbations in the mesosphere/lower thermosphere were the result of the secondary waves generated by the dissipation of the primary gravity waves from the volcanic eruption affirms the importance of higher-order wave generation. Furthermore, based on meteor radar observations of the gravity wave propagation around the globe, we estimate the eruption time to be within 6 minutes of the nominal value of 15th January 2022 04:15 UTC and localized the volcanic eruption to be within 78 km relative to the World Geodetic System 84 coordinates of the volcano confirming our estimates to be realistic.

1 Introduction

The Hunga Tonga-Hunga Ha‘apai (HTHH) volcano erupted on 15 January 2022, with the strongest eruption occurring at 04:15 UTC. This eruption injected a gigantic amount of water vapor into the stratosphere and mesosphere (Millán et al., 2022), generated a huge ash plume reaching up to 57 km in altitude (Carr et al., 2022), and launched Lamb waves and gravity waves into the atmosphere (Wright et al., 2022; Liu et al., 2023; Vadas et al., 2023a). Because of the very large amplitudes involved, this eruption provided a unique opportunity to study the gravity wave propagation around the globe throughout all atmospheric layers from the troposphere to the thermosphere and ionosphere. Many previous studies focused on the Lamb waves generated by the sudden and vigorous explosion of the volcano in the Pacific (Wright et al., 2022; Matoza et al., 2022; Liu et al., 2023). TEC observations around the Pacific region indicated strong ionospheric disturbances associated with the Hunga-Tonga eruption (Themens et al., 2022; Heki, 2022; Yamada et al., 2022; Zhang et al., 2022). Recent modeling and observations indicate that these disturbances seemed to be the result of secondary gravity wave generation rather than a direct propagation of the Lamb wave for which the upper mesosphere is an evanescent region due to the lower speed of sound (Vadas et al., 2023b; Stober et al., 2023). The more complicated propagation conditions in the mesosphere with the extremely cold mesopause and highly variable winds indicate why observations of the Hunga-Tunga eruption are underrepresented in the literature for this atmospheric layer. Wright et al. (2022) reported a signature of the Hunga-Tonga-caused waves over Hawaii seen in airglow. Meteor radar observations involving the Nordic Meteor Radar Cluster and the Chilean Observation Network De Meteor Radars



30 (CONDOR) indicated that the Lamb waves from the HTHH were attenuated in the mesosphere/lower thermosphere (MLT) and that the strongest amplitudes and signatures of the volcanic eruption were found as eastward and westward propagating gravity waves with intrinsic phase speed of about 210 m/s and horizontal wavelengths of 1600-2000 km (Stober et al., 2023). Simulations of the TEC disturbances in the ionosphere and thermosphere reveal how MLT winds affect the upper atmosphere through ExB-coupling (Miyoshi and Shinagawa, 2023; Shinbori et al., 2022). Such multistep vertical coupling, which results from the dissipation of primary GWs from HTHH in the thermosphere is important for explaining why the volcanic-caused waves have much higher phase speeds in TEC observations (Themens et al., 2022; Vadas et al., 2023b) and in MIGHTI (Michelson Interferometer for Global High-Resolution Thermospheric Imaging) neutral wind measurements in the thermosphere (Vadas et al., 2023a) as compared to the waves reported in the lower and middle atmosphere (Wright et al., 2022; Matoza et al., 2022; Stober et al., 2023). The HTHH event also provided a benchmark for the modeling of the volcano-triggered gravity waves and their global propagation in a variable background wind field. Simulations with the Ground-to-Topside Model of Atmosphere and Ionosphere for Aeronomy (GAIA) and the Whole Atmosphere Community Climate Model With Thermosphere and Ionosphere Extension (WACCM-X) modeled the GW and pseudo-Lamb waves and their propagation around the globe (Miyoshi and Shinagawa, 2023; Liu et al., 2023). In this study, we leverage the Model for gravity wave SOURCE, Ray tracing and reCONstruction (MESORAC)/High Altitude Mechanistic Circulation Model (HIAMCM) and demonstrate that concentric gravity wave structures generated by the HTHH eruption reached the thermosphere causing perturbations in the neutral winds as well as in the TEC (Miyoshi and Shinagawa, 2023; Vadas et al., 2023b, a).

In the present paper, we investigate the mesospheric propagation of the strongest gravity waves launched by the HTHH eruption using globally distributed meteor radar observations covering the latitudes from 79°N on Svalbard to 78°S at McMurdo, Antarctica. We identified these gravity waves in wind measurements using 13 different meteor radars at various distances from the eruption site, which allows us to infer the observed wave phase speeds for eastward and westward propagation with high accuracy. Furthermore, we demonstrate some asymmetries in the concentric gravity wave propagation, which led to characteristic amplitude variations at certain stations. Furthermore, we perform a similar analysis using HIAMCM wind data to compare the observational results with the model wind fields (Vadas et al., 2023a).

55 2 Meteor radar observations

Meteor radars have been used for decades to measure the winds and meteor flux in the MLT (Hocking et al., 1997, 2001; Holdsworth et al., 2004; Meek et al., 2013). The HTHH eruption presented an opportunity to demonstrate the capabilities of this technique to detect and trace GWs from a known source around the globe using a common and standardized analysis. On the other hand, the biggest challenge in processing the data from monostatic single station data is to achieve a temporal resolution of 10 min while still keeping a good altitude coverage of at least 10 km over the meteor layer. Considering the long vertical wavelength of the HTHH GWs, we kept the frequently used vertical resolution of 2 km but with a 5-kilometer vertical averaging window centered around the respective altitude. On the other hand, a temporal averaging of more than 10 minutes



substantially weakens the volcanic gravity wave signature and, thus, reduces the probability of identifying the HTHH GWs in the wind measurements.

65 We identified the HTHH GWs collecting data from 13 meteor radars around the globe. The meteor radars are located at Mc-Murdo (McM) (Marino et al., 2022), Davis (DAV), Rothera (ROT) (Dempsey et al., 2021), in Argentina the Southern Argentina Agile Meteor Radar (SAAMER) Tierra del Fuego (TDF) (Fritts et al., 2010), CONDOR represented by the Andes Lidar Observatory (ALO) (Stober et al., 2021b), Cariri (CAR) (Andrioli et al., 2013), Canadian Meteor Orbit Radar (CMOR) (in this study also - CMO) (Webster et al., 2004; Brown et al., 2010), Pokerflat (PKF), Mengcheng (MEN) (Yang et al., 2023), Kun-
70 ming (KUN) (Zeng et al., 2022), Svalbard (SVA) (Hall and Tsutsumi, 2020), the Nordic Meteor Radar Cluster (NORDIC) represented by the Tromsø (TRO) (Hall and Tsutsumi, 2013; Stober et al., 2021b) and Collm (COL) (Jacobi et al., 2007). The Nordic Meteor Radar Cluster data was reduced to be equivalent to a monostatic meteor radar located at the reference coordinate, which is close to Tromsø. All monostatic meteor radars were analyzed by applying a retrieval algorithm including the World Geodetic Reference System (WGS84, (National Imagery and Mapping Agency, 2000)), to compute the East-North-Up
75 coordinates at the geographic location of each detected meteor. Non-linear error propagation was considered to incorporate the spatial and temporal wind shears within each time-altitude bin (Gudadze et al., 2019; Stober et al., 2021a). More details of the implementation could be found in Stober et al. (2021b, 2022). Figure 1 shows a map visualizing all meteor radar locations. The blue lines indicate the shortest great circle (GC) distance between each meteor radar and HTHH. The dashed red line indicates the full GC that connects ALO and HTHH. The yellow line indicates the long GC path along the eastward direction
80 connecting HTHH to the European radars. The lines indicate idealized propagation paths of the secondary GWs caused by the eruption and are used to measure the distances. The distances shown in the map are computed at 90 km altitude to account for the mesospheric propagation.

The meteor radars used in this study provide good coverage around the Pacific to investigate potential differences or asymmetries of the volcano-triggered GWs. Furthermore, four stations, namely MEN, KUN, ALO, and CAR are located very close to
85 the same GC (dashed red line) and, thus, it is straightforward to infer differences in the eastward and westward propagation of the GWs. A summary of all stations with their geographic coordinates and their eastward and westward GC distances from the HTHH eruption site are summarized in Table 1.

3 HIAMCM global fields

The HIAMCM is a gravity wave-resolving General Circulation Model (GCM) from the surface to about 450 km altitude. A
90 detailed description of the HIAMCM is found in Becker and Vadas (2020). Recently, it was demonstrated that the HIAMCM can be nudged to meteorological reanalysis such as The Modern-Era Retrospective Analysis for Research and Applications (MERRA-2). The nudging is implemented in the spectral domain, which allows to specify realistic large-scale meteorological fields for the resolved GW (Becker et al., 2022). Leveraging these new capabilities, the primary and secondary GWs resulting from the HTHH eruption were simulated with MESORAC and the HIAMCM, respectively, and were analyzed to study the im-
95 pact of the volcanic eruption on the thermospheric-ionospheric system (Vadas et al., 2023b, a). Here, the MESORAC simulated

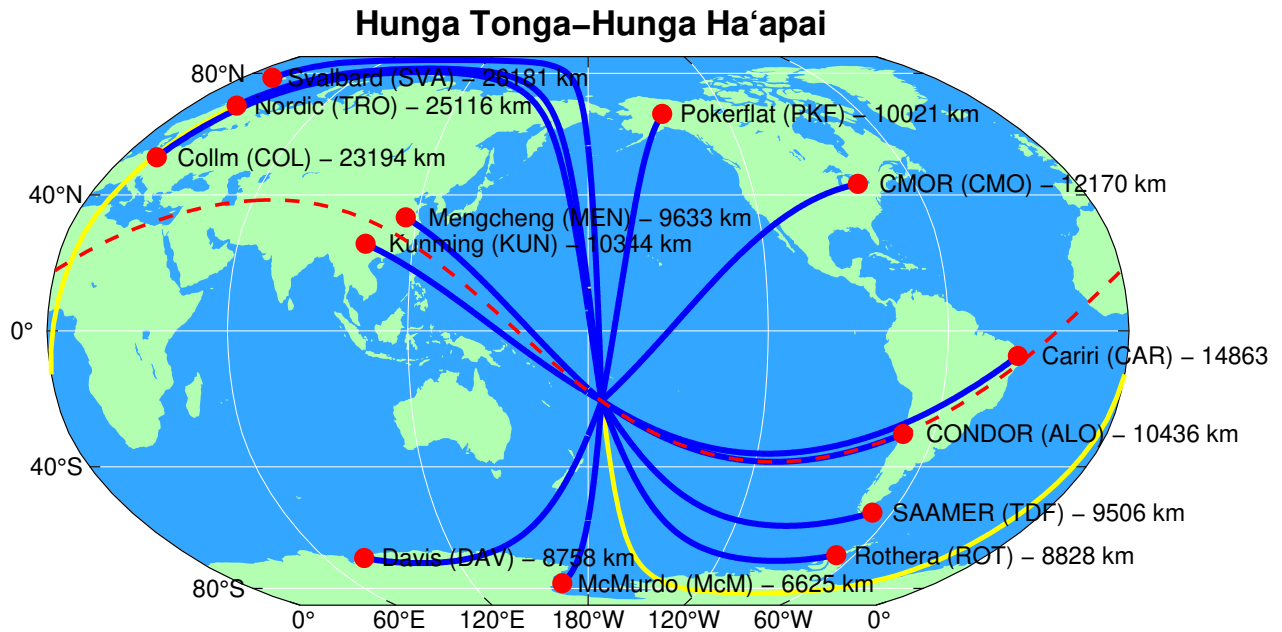


Figure 1. Robinson projection of the globe centered on the Pacific. The solid blue lines show the shortest GC distance between the volcanic eruption and the center of each station. The solid yellow line reflects the long GC path for the European radars. The dashed red line indicates the full GC path connecting the volcano and ALO, CAR, MEN, and KUN.

the excitation, propagation, and dissipation of the local primary GWs created from the vertical updrafts of air in the stratosphere identified from GOES-17 satellite images. The local body forces and heatings created where the primary GWs dissipated were then input into the HIAMCM, which subsequently generated the secondary GWs that propagated globally. The updrafts used for the input in MESORAC reached altitudes of $z > 50$ km (Carr et al., 2022), but the ray tracing of the GWs was launched at $z = 30$ km and occurred within 1 hour 30 min after the first eruption and were cover longitudes between $176.5 - 175.5^\circ$ W and latitudes between $21 - 20.4^\circ$ S (Vadas et al., 2023a).

In this study, we focus on the mesospheric data from the HIAMCM between 80-100 km and with a temporal resolution of 5 minutes using the model runs from Vadas et al. (2023a). The simulated perturbations are defined as the differences between the results from the "Tonga run" (with inputs from MESORAC) and the "base run" (without inputs from MESORAC). The HTHH GWs are extracted by subtracting a reference run from the disturbance simulation. Furthermore, we apply an observational filter for each meteor radar to account for the spatial and temporal sampling of these radars similar to previous studies (Pokhotelov et al., 2018; Stober et al., 2020, 2021c).

Figure 2 shows maps of how the HTHH secondary GWs propagated around the Earth at 4 different times on the 15th of January 12 UT, 16 UT, 20 UT, and 24 UT. Note that each panel in Fig. 2 consists of an upper and a lower part that shows the zonal and the meridional winds, respectively. The HIAMCM GWs clearly propagate radially away from the HTHH eruption



	latitude	longitude	GC (short) / km	GC (long) / km
McM (McMurdo)	77.85°S	166.72°E	6626 (W)	33404 (E)
DAV (Davis)	68.58°S	77.97°E	8759 (W)	31271 (E)
ROT (Rothera)	67.57°S	68.12°W	8828 (E)	31202 (W)
TDF (Tierra del Fuego)	53.79°S	67.75°W	9505 (E)	30525 (W)
MEN (Mengcheng)	33.4°N	116.0°E	9634 (W)	30398 (E)
KUN (Kunming)	25.6°N	103.0°E	10345 (W)	29685 (E)
ALO (CONDOR)	30.3°S	70.7°W	10436 (E)	29594 (W)
CAR (Cariri)	7.38°S	36.53°W	14862 (E)	25168 (W)
PKF (Pokerflat)	65.13°N	147.5°W	10020 (E)	30010 (W)
CMO (CMOR)	43.26°N	80.77°W	12169 (E)	27861 (W)
SVA (Svalbard)	78.17°N	15.99°E	13848 (W)	26182 (E)
TRO (Nordic)	67.9°N	21.1°E	14913 (W)	25117 (E)
COL (Collm)	51.31°N	13.0°E	16836 (W)	23194 (E)

Table 1. Summary of the geographic locations for each meteor radar and GC distances relative to HTHH. The term short/long refers to the shortest/longest distance along the GC. The brackets after the GC distance indicate whether the westward or eastward HTHH GWs reached the station along this path.

115 site. However, the model also reflects a substantial radial asymmetry in the GW amplitudes indicating that the eruption resulted in different wavefronts for different azimuthal directions. The largest amplitudes are found for the southeastward propagation (towards the Andes and the Antarctic Peninsula), whereas much smaller GW amplitudes were simulated over Australia, China, and the North American sector. This asymmetry is due to the wind filtering of the primary HTHH GWs in the lower-middle atmosphere (stratosphere), which created primarily northward-southward local body forces (i.e., horizontal accelerations) from the momentum by the primary GWs, as discussed in Vadas et al. (2023a). Such body forces do not excite secondary GWs perpendicular to the primary GW propagation direction, and therefore create an asymmetric distribution of secondary GWs (Vadas et al., 2003; Vadas and Becker, 2018).

120 In addition, some of the additional azimuthal GW asymmetries may be due to the complex eruption sequence (Vadas et al., 2023a). Results from the HIAMCM also show that the HTHH GWs traveling westward along the GC towards Europe are disturbed by the polar vortex in the northern hemisphere and, thus, almost no coherent wavefront arrives over Scandinavia, although this would have been the shortest distance to HTHH. On the other hand, the HIAMCM results suggest that the most coherent wavefront from HTHH propagated towards South America and even gained strength over the Atlantic Ocean before reaching central Europe. This is consistent with the observations presented in Stober et al. (2023).

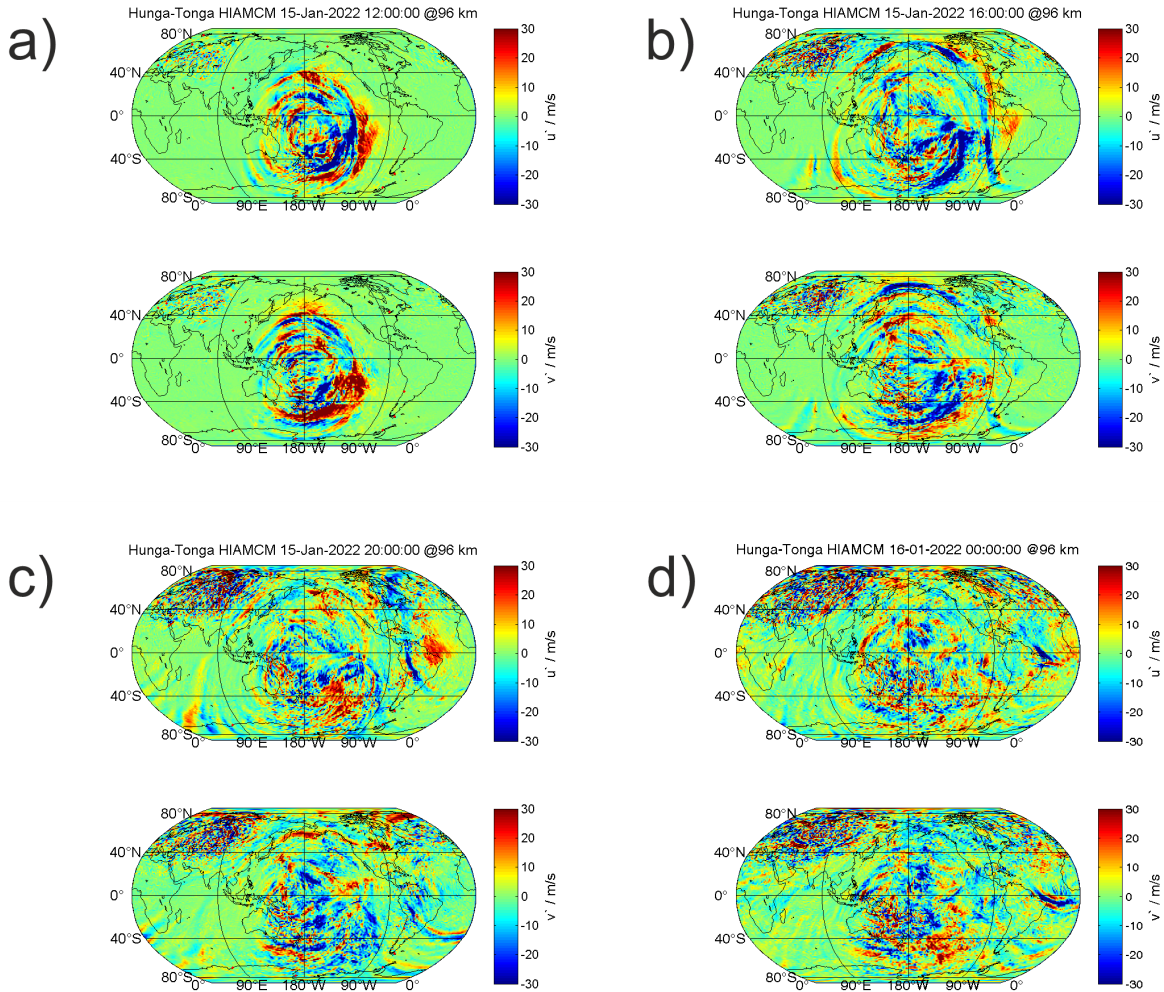


Figure 2. HIAMCM zonal wind perturbations u' (upper panel) and meridional wind perturbations v' (lower panel) from 15th January 2022 at 12, 16, 20, and 24 UT (a-d).

125 4 HIAMCM and meteor radar

Tracking the HTHH secondary GWs around the globe from meteor radar wind observations requires identifying the whole GW packet rather than one distinct feature that can be found in all observations. The main eruption lasted 3 hours and consisted of many vigorous detonations resulting in updrafts (Vadas et al., 2023a) triggering the HTHH primary GW field. The secondary GWs were generated by the local body forces created by the dissipation of the primary GWs in the mesosphere and thermosphere. Considering the HIAMCM simulation of the HTHH GW packet illustrates that there is a huge variety of
130 possible amplitudes and shapes of the GW packet depending on the different GC paths along which the waves are propagating.



Furthermore, derived phase velocities will depend on the ability to detect the leading edge of the HTHH GW packet, rather than on the maximum amplitude, which often corresponds to a later time of the eruption sequence, to identify the correct arrival time in the observation volume. Thus, the time of arrival estimates are prone to large uncertainties that have to be considered
135 in the further analysis of HTHH GWs. In the following, we briefly outline the analysis procedure.

We examined the 10 min resolution meteor radar winds and subtracted a 4-hour running window to remove traveling planetary waves (mostly the Quasi-2-Day-Wave (Q2DW) in the southern hemisphere), atmospheric tides, and GWs with observed periods longer than 4 hours. The vertically integrated anomalies were then inspected to identify the HTHH GW packet by searching for peaks in the zonal, meridional, and total horizontal wind speed. Our observations can be grouped into three different classes
140 depending on the shape of the GW packet, the amplitude, or a superposition with other waves. The timing was then estimated for all stations that showed a sinusoidal wave by the onset of the GW packet. Typical examples of these stations are ALO, PKF, and TDF. For the other stations, we searched for the first GW amplitude peak in an interval around the estimated arrival time e.g., CMOR, McM, and DAV.

Figure 3 compares the theoretical arrival times of the wave packet leading edge for all meteor radars (left column) and HI-
145 AMCM winds from Tonga run minus base run (right column) from the Antarctic Peninsula to Alaska. The time of the first eruption is shown as a yellow vertical line. The cyan vertical lines indicate the arrival times of the eastward propagating HTHH GW packet estimated from the best-fit phase speed using all stations that detected this wave, whereas the black vertical lines show the best fit of the arrival time of the westward wave. The dashed vertical red lines show the one-sigma range of the leading edge arrival time for each station. The y-axis for the HIAMCM winds is reduced by a factor of 4 to compensate for the smaller
150 wind amplitudes in the model when comparing the difference between the Tonga run and the base run. The observations and the HIAMCM show a remarkable agreement for several stations in both the timing and wave pattern at ALO, PKF, or CAR. Only CMOR exhibits a visible difference in the observed arrival time compared to HIAMCM. Although CMOR is one of the most powerful systems, concerning the number of meteors detections and wind altitude coverage used in this study, the HTHH GW is barely identifiable in the zonal wind component; the observations indicate a much less clear wavefront and an earlier
155 arrival time compared to the model and in relation to the other stations.

The comparison of the wind anomalies of the Antarctic stations of McM and DAV and the two radars located in China (MEN and KUN) are presented in Figure 4. Although the two meteor radars on the Antarctic continent are located at the closest distance to HTHH, the GW signature is barely visible in the data. The HTHH GW is mainly identified by a coherent sinusoidal signature (between the vertical lines), which was also found in other stations. However, the amplitude of this wave signature
160 does not exceed the background atmospheric signal for these two stations. Furthermore, these two stations also reflect the largest discrepancy in the arrival time between the observations and HIAMCM (see next section). Interestingly, KUN and MEN meteor radars observed the HTHH GW with a much smaller amplitude than their counterparts eastward of the volcano in South America (ALO, and CAR), even though all these stations are roughly on the same GC. The increased variability in the wind anomalies prior to the HTHH in the meteor radar data is mainly due to the diurnal variation in the meteor count
165 rate, which reached a minimum during these times. This provides observational confirmation of the asymmetric azimuthal propagation found in the HIAMCM zonal and meridional wind perturbations. Another important aspect is that the zonal and

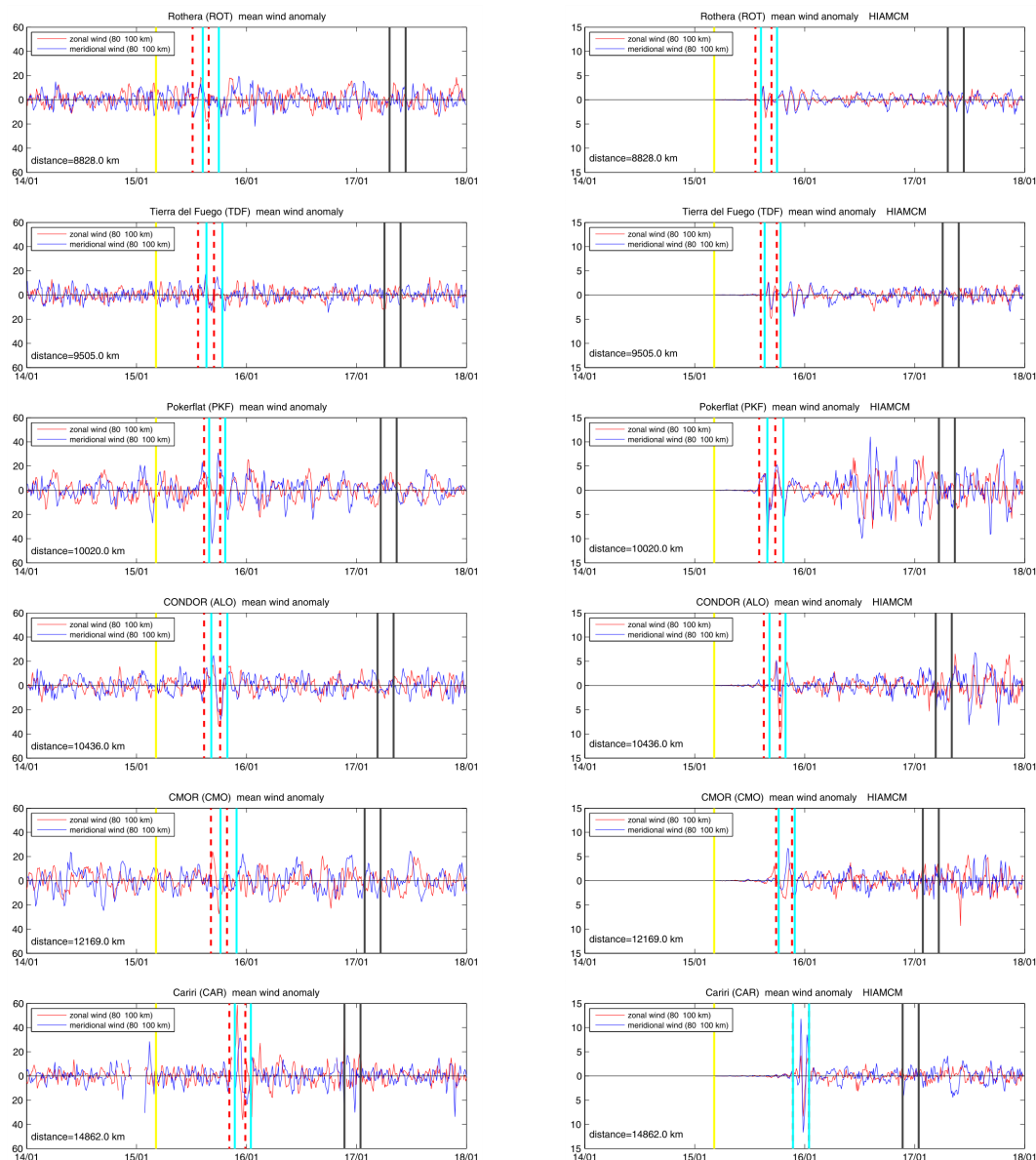


Figure 3. Wind anomalies for the meteor radars located eastward of HTHH and corresponding anomalies from HIAMCM. The date ticks are given at 00:00 UTC of the date. The time of the volcanic eruption is indicated by a vertical yellow line. The cyan vertical lines span the predicted arrival of the eastward propagating GW. The black vertical lines indicate the timing for the westward propagating HTHH GW packet. The dashed vertical lines indicate the one-sigma interval of the time picks for each station. Note that the HIAMCM shows perturbations only to the right of the yellow line because we plotted the differences between the Tonga run and the base run (see Sec. 3).



meridional winds were out of phase for the MEN and KUN stations, indicating a northwestward propagation, whereas CAR and ALO exhibit an in-phase relationship between the two wind components, which is expected for eastward propagating. Also, the arrival times between the HIAMCM and the Chinese meteor radars are in much better agreement compared to McM and DAV.

Wind anomalies above the European sector are shown in Figure 5. We identified the eastward propagating GWs (long GC

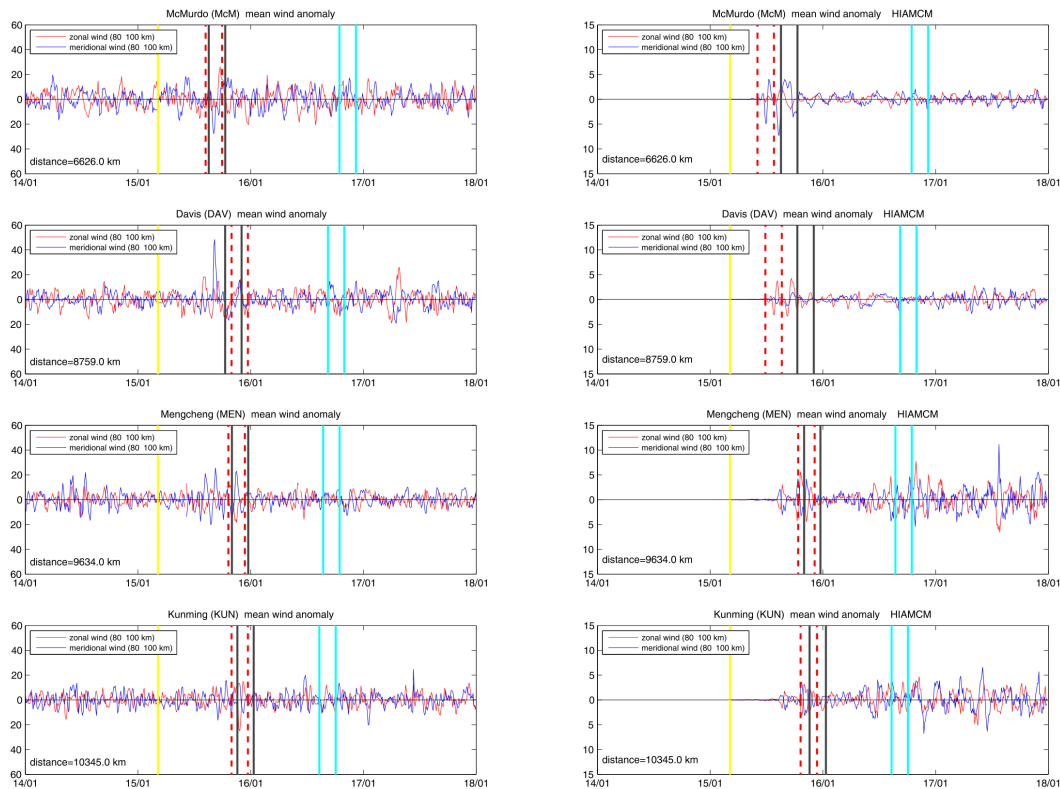


Figure 4. The same as Figure 3, but for the stations westward of HTHH outside the European continent.

path) by searching for identical patterns in the wind anomalies for all three stations. The cyan vertical lines mark a coherent wave structure that exhibits an in-phase behavior of the zonal and meridional winds (as expected since the GWs are propagating northeastward), similar to what was found for all the South American stations, but with a 180-degree phase shift. HIAMCM winds also show some remnants of the eastward HTHH GW over the European sector. Overall, the data is much noisier in the northern hemisphere winter due to GWs from orographic forcing and the polar vortex. The increased variability, compared to pre-HTHH-eruption time, in the observations may be due to the generation of GWs created by seeding of GWs by the Lamb wave that arrived a few hours before the HTHH GWs (Stober et al., 2023). In addition, we note that Lamb waves likely create a continuum of GWs. For the HTHH Lamb waves the seeding process seems to occur at or above $z \simeq 110$ km (Vadas et al., 2023b).

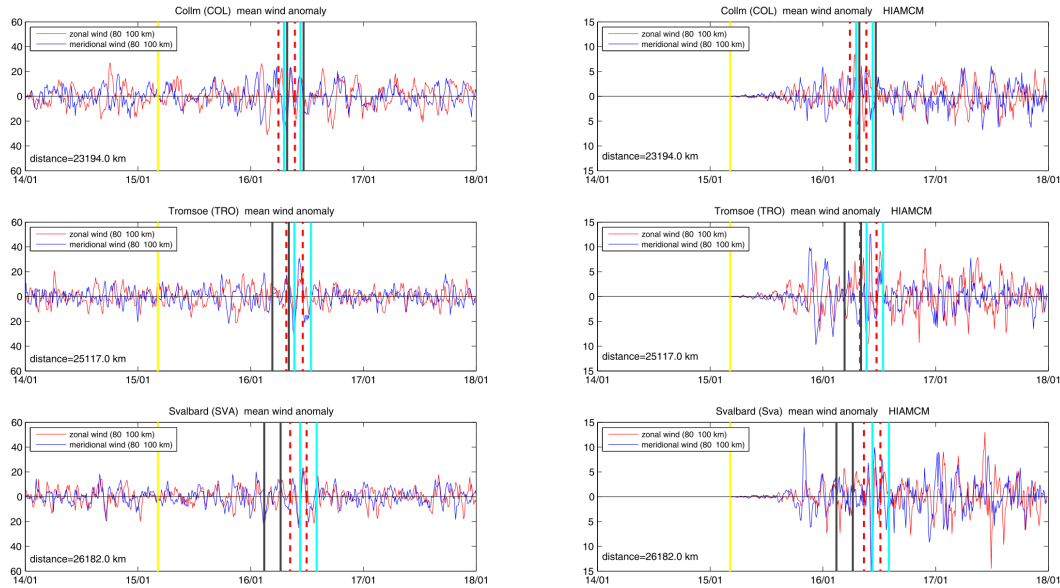


Figure 5. The same as Figure 3, but for the European meteor radar sites.

5 Gravity wave observed phase speeds

Gravity wave phase speeds are derived from all meteor radar stations using the times of arrival for each individual station. The phase speeds of the GW packet with the largest amplitude are determined by fitting a distance vs. time and time vs. distance to account for errors in the time estimates as well as for the sizes of the observation volumes. We assumed a 3-hour uncertainty
 185 for the time corresponding to the most active part of the eruption sequence. The spatial uncertainty is given by the diameter of the observation volume and we used 350 km for all stations.

Figure 6 shows four panels summarizing the analysis. The left column presents the meteor radar observations and the right column presents the HIAMCM data. The observational data can be grouped in an eastward wave (red line) with an observed phase speed of 240 ± 5.7 m/s and a westward traveling GW (blue line) exhibiting an observed phase speed of 166 ± 6.4 m/s. The
 190 fits were obtained by separating the stations according to their relative position (eastward or westward) of HTHH. The eastward stations of ROT, TDF, ALO, PKF, CMOR, CAR, COL, TRO, and SVA provide enough data to determine the eruption time to be within 6-12 min and eruption location to be within 80 km of the nominal HTHH coordinates in the WGS84 reference. The precision of the fitting coefficients significantly depends on the European stations. Due to the much larger distance and time between the eruption, the errors of the individual measurements are less critical. The westward wave (blue) was analyzed using
 195 a regularized fit. The fit is regularized by a fixed eruption time $t_0 = 0$ hours and by a fixed location using the nominal HTHH coordinate. This strategy is necessary to account for the much smaller number of observations. The relative distance between DAV, KUN, and MEN and the volcano is almost identical leaving essentially only McM as a second point. Thus, we added the westward HTHH wave signature that was found in the ALO and already presented in Stober et al. (2023) to the fit.



The same analysis is applied to HIAMCM and the fitted observed phase velocities for the eastward and westward HTHH GW are in very good agreement between the model and the observations. Only the Antarctic stations of McM and DAV show a substantial deviation. The Q2DW may play an important role and is clearly visible in the southern hemisphere at mesospheric altitudes in the meteor radar data (Stober et al., 2023). However, there is no indication of this wave found in MERRA2 and, thus, due to the nudging of the large-scale dynamics in HIAMCM from re-analysis, it is also missing in the HIAMCM winds. The amplitude of the Q2DW is strongest in the meridional wind component and showed a clear northward wind direction during the time of eruption above the South American continent. Climatological studies of the Q2DW have shown that the wavenumber 3 often dominates in the southern hemisphere around 30°S, which suggests that the HTHH GW-packet faced a strong headwind towards the south (Iimura et al., 2021). This explains the different arrival times of the HTHH GW packet at McM and DAV and why the signatures for these stations are less clear, although these stations are closer to the eruption compared to many other meteor radars used in this study. We did not investigate a possible Q2DW activity for the northern hemisphere, although this wave is sometimes found also at polar latitudes during winter (Nozawa et al., 2003).

Finally, Figure 7 compares the derived observed phase speed for each station separately relative to the distance along the GC path from the radars (left panel) and the HIAMCM (right panel). The ALO station is added with both detections (eastward and westward GW packet) of the HTHH GW and, thus, appears at two distances representing the eastward and westward GC distance. There is a remarkable agreement for ALO, SVA, TRO, CAR, COL, MEN, and KUN to within ± 5 m/s when comparing the HIAMCM to the observations. Furthermore, this comparison confirms that there are two clusters that correspond to the eastward (240 m/s) and westward (160 m/s) HTHH GW packets. It is also obvious that the observed phase speeds remain roughly constant with distance from the volcano. The reasons for the exceptional behavior of DAV and McM in the HIAMCM data are already discussed.

6 Discussion

Although meteor radars have become a widely used sensor to observe mesospheric winds, there have been almost no studies on the HTHH eruption based on such observations. Identifying the HTHH GW in standard monostatic meteor radars turned out to be more challenging than would be expected from the stratospheric data (Wright et al., 2022) and only became feasible due to the results obtained from the high-resolution analysis with the 3DVAR+DIV algorithm (Stober et al., 2023) using MRs with high meteor detection rates such as CONDOR and the Nordic Meteor Radar Cluster. Motivated by this original study, Poblet et al. (2023) aimed to identify the HTHH-caused Lamb wave in hourly winds derived from CONDOR and other South American meteor radar networks. However, such a temporal resolution appears to be insufficient to unambiguously identify the HTHH-Lamb wave considering the wave properties presented in Liu et al. (2023). The HIAMCM simulations used for comparison to the radar observations are found to produce a much more fragmented wavefront for the volcanic-caused GWs, including different GW amplitudes for different azimuths relative to the eruption site (Vadas et al., 2023a) when compared to a high-resolution WACCM-X simulation of the pseudo-Lamb wave modes (Liu et al., 2023).

Previous publications emphasized the Lamb waves generated during the first eruption (Wright et al., 2022; Matoza et al.,

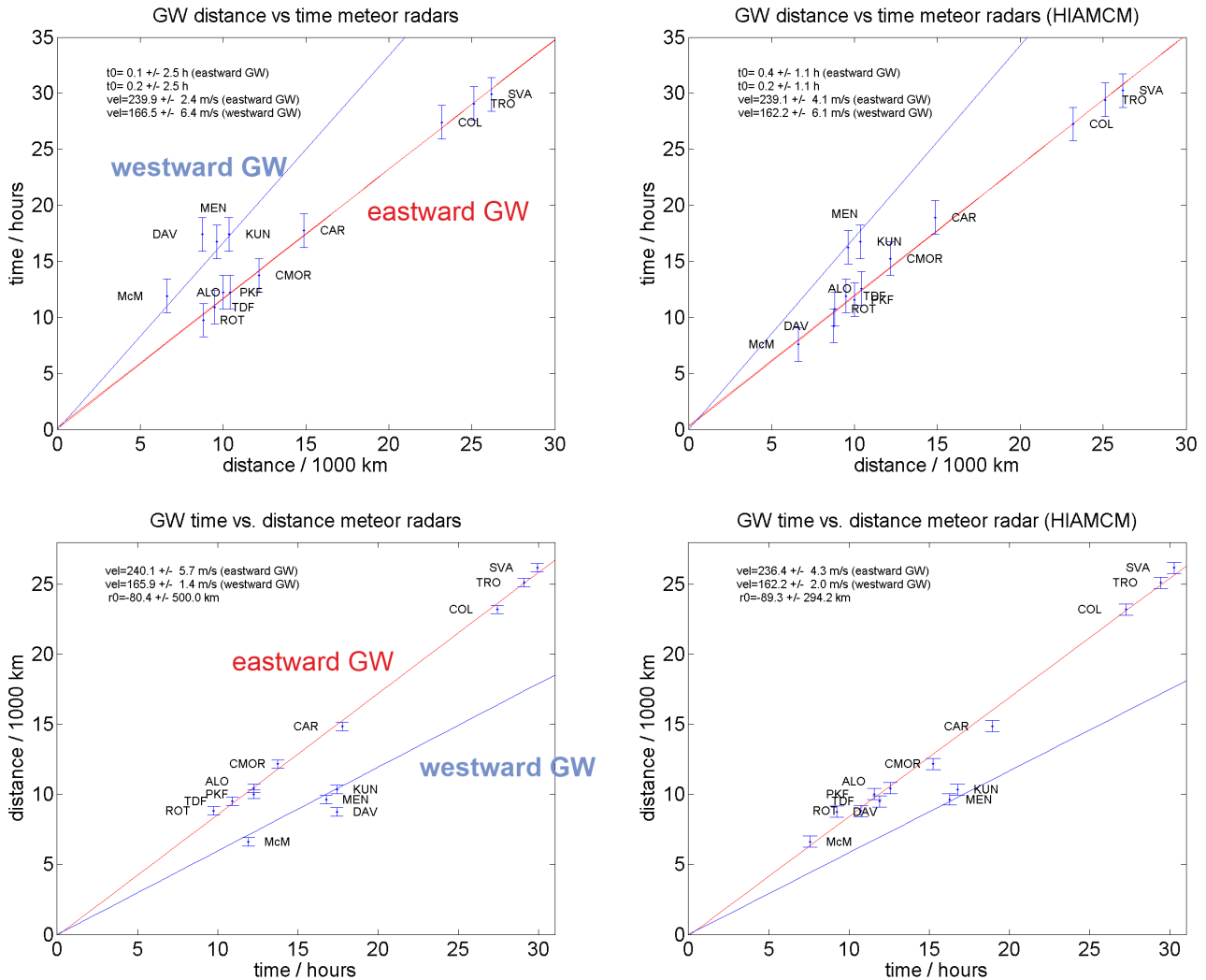


Figure 6. Gravity wave phase speed analysis for the meteor radars (left column) and HIAMCM (right column) as distance versus time and time versus distance plots. The red line indicates the best fit for the eastward propagating HTHH GW, the blue line is the best fit for the westward propagating HTHH GW.

2022), which was observable in surface pressure data and stratospheric brightness temperatures observed by satellites. However, high-resolution wind measurements indicated only weak signatures of a possible Lamb wave in the MLT below 90 km altitude (Stober et al., 2023). Upon reaching the GW seeding altitude of $z \approx 110$ km, the small-amplitude Lamb waves could have seeded a continuous spectrum of upward and downward-propagating weak-amplitude GWs similar to the GW spectrum excited at the surface by a localized ocean wave packet such as a tsunami (Vadas et al., 2015). The small-amplitude Lamb waves in the MLT could be the source of the enhanced GW activity before the HTHH eastward GW actually arrived in the

235

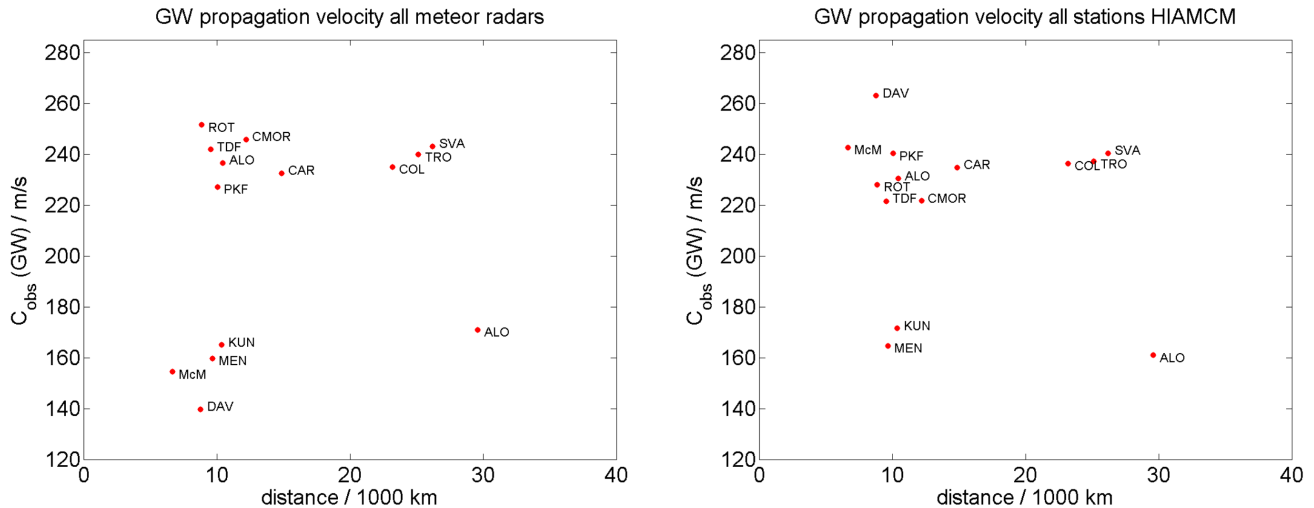


Figure 7. Comparison of individual observed phase velocities for the meteor radars and HIAMCM.

observation volume (Stober et al., 2023). Similar observations can be made for the MEN and KUN meteor radars in China, which also reveal an increased variability before the westward HTHH GWs arrived (see Figure 5, and 4).

240 The observed phase velocities derived in the present study depend crucially on how the timing is determined and referenced. In the literature, typically the onset of the HTHH eruption sequence is used as a reference (15th January 04:15 UTC). However, this captures only partially the complexity of the eruption sequence, which lasted for about three hours and consisted of several vigorous explosions. We accounted for this complexity by always representing the HTHH GW packet by vertical lines where the left one refers to the onset and the right one is given by onset +3 hours. This is important for the comparison with HIAMCM
 245 where 5 primary volcanic eruptions are modeled with different launch times spread over 1 hour 30 min after the initial primary explosion (Vadas et al., 2023a). Furthermore, there is a longitudinal and meridional shift of the location of the updrafts from GOES-17 of about 0.7° or about 70-90 km, and the nominal geographic coordinates of the volcano (175.38° W, 20.54° S), which we used as a reference to compute the distances. Considering these aspects demonstrates how precisely the t_0 -time and also the location of the eruption have been inferred from the global meteor radar data.

250 A key factor for the propagation of the GWs is the speed of sound because it forms an effective natural altitude-dependent bottleneck or barrier. Since most of the large-amplitude secondary GWs were created at $z \approx 120$ -150 km (e.g., Fig. 13 of Vadas et al., 2023b), those that propagate through the MLT are downward-propagating. The mesopause region typically has a sound speed of $c_s \approx 280$ m/s, which results in a maximum intrinsic horizontal phase speed of $c_s \approx 250$ m/s (Vadas and Azeem, 2021). This is consistent with the maximum observed phase speeds of 240 m/s of the HTHH GWs in the MLT. In addition, the eruption
 255 occurred during the southern hemispheric summer, where temperatures below 140 K are expected, which was confirmed by the presence of Noctilucent clouds in Tierra del Fuego. These temperatures for the lower southern latitudes around the Antarctic continent are consistent with a speed of sound limit close to approximately 239 m/s (Stober et al., 2023), which results in a



maximum intrinsic horizontal phase speed of $0.9c_s \simeq 215$ m/s. This threshold is very likely the reason why the MLT winds at DAV and McM did not show a large amplitude or clear wave pattern of the HTHH GWs at both sites, although both stations
260 are located at the closest distance to HTHH of all meteor radars included in our study. However, the HIAMCM predicted that McM and DAV would observe HTHH GWs with observed phase speeds of about 240 m/s. As mentioned previously HTHH GW packet was Doppler shifted due to a strong Q2DW activity in the southern hemisphere (Stober et al., 2023), which was also found in ROT, TDF, McM, and DAV (data not shown) and, thus, explains the differences in the arrival times between the observations and HIAMCM. However, it also confirms that the intrinsic wave speed was much closer to the sound speed barrier
265 and, thus, forced the HTHH GWs to reflect, thereby preventing the GWs from entering the Antarctic polar MLT region. Hence, the HTHH GWs signatures in the MLT winds found above McM and DAV appear to be much weaker.

Comparing the observations from MEN, KUN, ALO, and CAR confirms findings presented in a previous study about the intrinsic wave properties of the HTHH GW traveling along the GC (Stober et al., 2023). All four stations are located rather close to the same GC and, thus, are suitable to evaluate the results obtained from the high-resolution 3DVAR+DIV retrievals
270 (Stober et al., 2023). Hence, our present study confirms that the HTHH GW packet had an intrinsic wave speed of 202.5 m/s along this GC. This velocity is low enough to not be affected by the speed of sound limitation caused by a too-cold mesopause somewhere along the GC, which is confined between 40° S and 40° N. This might also explain why only the 3DVAR+DIV analysis at CONDOR revealed the signatures of both the eastward and westward HTHH GW packets.

Simulations of the Lamb wave modes L0 and L1 with WACCM-X suggest that the L1 has a phase speed of about 240 m/s (Liu
275 et al., 2023). Although this phase speed seems to agree with the observed phase speeds in this study, the observed horizontal wavelength of about 1600-2000 km (Stober et al., 2023), and a wave period of 2 hours 20 min cannot be reconciled with the Lamb waves properties. Furthermore, HIAMCM and meteor radar zonal and meridional winds exhibit variable phase relations between both wind components and a much less coherent phase front than expected for a Lamb wave. There might have been an L1 mode in the MLT, but such a wave was hardly visible in the available meteor radar wind data. Also, note in this context
280 that the spatial averaging of 350 km in diameter and temporal resolution of 10 min clearly sets limits for the observed radar winds to reflect Lamb wave perturbations.

7 Conclusions

In this study, we analyzed winds from 13 globally distributed meteor radars to track HTHH GW packets in the eastward
285 and westward directions from the volcano. The observational data was compared to HIAMCM simulations. This allowed us to identify the HTHH GWs in the observations and applied the same observational filter to the HIAMCM. We were able to track eastward propagating HTHH GWs for 30000 km from the eruption site in the Pacific up to the Arctic over Svalbard. We determined an observed horizontal phase velocity of 240 ± 5.7 m/s. Furthermore, we found westward propagating HTHH GWs with an observed horizontal phase speed of 166.5 ± 6.4 m/s. The observed phase speeds are in excellent agreement with
290 HIAMCM, which showed observed phase speeds of 239.5 ± 4.3 m/s and 162.2 ± 6.1 m/s for the eastward and westward GWs,



respectively.

The joint analysis of the global meteor radar observations and HIAMCM perturbations demonstrate the interplay between data and simulations, with both informing each other helping to understand the complex dynamical situation caused by the HTHH eruption. The model data provided global information about the HTHH GW propagation, which confirmed that the European meteor radars observed the eastward GW as the strongest signature of the HTHH eruption at the MLT. On the other hand, the observations also revealed that the Q2DW played an important role in the propagation along different GC. Furthermore, the MR observations alone are not sufficient to distinguish between primary and secondary GW generated by HTHH. However, the modeled HIAMCM secondary waves explain very well the observed phase speed and propagation direction and, thus, there is some confidence that indeed these GWs were forced due to the dissipation of primary waves.

The comparison between the meteor radar winds and corresponding model results illustrates the capability of HIAMCM to model the HTHH GWs and their propagation over long distances. The HTHH eruption provided an ideal benchmark for evaluating and comparing observations and models regarding the global dynamics of GWs from a spatially and temporally confined source region. The HIAMCM result revealed the very complex structure of the wavefront generated by the HTHH eruption in the MLT with its large variations of the background flow for GWs from tides and traveling PWs as opposed to the situation observed in the stratosphere (Wright et al., 2022).

Tracking the eastward HTHH GW in the meteor radar winds made it possible to determine the GW generation time to be within 6 min of the nominal eruption time (15th Jan 2022 04:15 UTC) and the location was found to be within a range of 78 km to the WGS84 coordinates of the volcano. Both values are in good agreement with HIAMCM and within derived statistical uncertainties. Furthermore, the obtained accuracy of the determination of the eruption location from HIAMCM is quite satisfactory when considering the complexity of the eruption sequence modeled with MESORAC, which is based on GOES-17 updrafts. These updrafts extend over 0.7° in longitude and showed a horizontal distance of up to 70 km from the volcano WGS84 coordinates. Only the secondary GWs that resulted from the ambient flow effects that occurred when the updraft-induced primary GWs dissipated were simulated by the HIAMCM and, hence, these secondary GWs (not the primary GWs) propagated around the globe and can explain the majority of the analyzed worldwide radar wind GW perturbations in response to the HTHH eruption.

Author contributions. The meteor radar data analysis was performed by GS. HIAMCM runs were carried out by SLV and EB. The data interpretation was done by GS, SLV, EB, JC, DM, SN, and KB. All authors contributed to the editing of the manuscript. The operation of the meteor radars was secured by all instrument PIs.

Competing interests. All authors declare that there are no competing interests.



320 *Disclaimer.* Any opinions, findings, and conclusions or recommendations expressed in this material are those of the author(s) and do not necessarily reflect the views of the National Science Foundation.

Acknowledgements. Gunter Stober, Witali Krochin and Guochun Shi are members of the Oeschger Center for Climate Change Research (OCCR). Witali Krochin and Guochun Shi are supported by the Schweizerischer Nationalfonds zur Förderung der Wissenschaftlichen Forschung (grant no. 200021-200517 / 1).

325 SLV and EB were supported by NSF grant # AGS-1832988.

Alan Liu is the CONDOR instrument PI and his work is supported by (while serving at) the National Science Foundation (NSF), USA. Zishun Qiao and the operation of the CONDOR meteor radar system are supported by the NSF grant AGS-1828589.

The Esrange meteor radar operation, maintenance, and data collection were provided by the Esrange Space Center of the Swedish Space Corporation.

330 This research has been supported by the STFC (grant no. ST/W00089X/1 to Mark Lester).

This study is partly supported by Grants-in-Aid for Scientific Research (no. 21H04516, 21H04518, 21H01144, 20K20940) of the Japan Society for the Promotion of Science (JSPS).

Federal University of Paraíba (UFPB) for facilities to install and operate the Cariri meteor radar.

335 Njål Gulbrandsen acknowledges the support of the Leibniz Institute of Atmospheric Physics (IAP), Kühlungsborn, Germany for their contributions to the upgrade of the TRO meteor radar.

Operation of the Davis meteor radar was supported by Australian Antarctic Science projects 4445 and 4637. Support for DJ as well as SAAMER-OS' operation are provided by NASA's Planetary Science Division Research Program, through ISFM work packet Exospheres, Ionospheres, Magnetospheres Modeling at Goddard Space Flight Center and NASA Engineering Safety Center (NESC) assessment TI-17-01204. This work was supported in part by the NASA Meteoroid Environment Office under cooperative agreement no. 80NSSC21M0073.

340 The work by Wen Yi is supported by the National Natural Science Foundation of China (grants No. 42174183).



References

- Andrioli, V. F., Fritts, D. C., Batista, P. P., and Clemesha, B. R.: Improved analysis of all-sky meteor radar measurements of gravity wave variances and momentum fluxes, *Annales Geophysicae*, 31, 889–908, <https://doi.org/10.5194/angeo-31-889-2013>, 2013.
- Becker, E. and Vadas, S. L.: Explicit Global Simulation of Gravity Waves in the Thermosphere, *Journal of Geophysical Research: Space Physics*, 125, e2020JA028034, <https://doi.org/https://doi.org/10.1029/2020JA028034>, e2020JA028034 10.1029/2020JA028034, 2020.
- 345 Becker, E., Vadas, S. L., Bossert, K., Harvey, V. L., Zülicke, C., and Hoffmann, L.: A High-Resolution Whole-Atmosphere Model With Resolved Gravity Waves and Specified Large-Scale Dynamics in the Troposphere and Stratosphere, *Journal of Geophysical Research: Atmospheres*, 127, e2021JD035018, <https://doi.org/https://doi.org/10.1029/2021JD035018>, e2021JD035018 2021JD035018, 2022.
- Brown, P., Wong, D., Weryk, R., and Wiegert, P.: A meteoroid stream survey using the Canadian Meteor Orbit Radar: II: Identification of minor showers using a 3D wavelet transform, *Icarus*, 207, 66–81, <https://doi.org/https://doi.org/10.1016/j.icarus.2009.11.015>, 2010.
- 350 Carr, J. L., Horváth, A., Wu, D. L., and Friberg, M. D.: Stereo Plume Height and Motion Retrievals for the Record-Setting Hunga Tonga-Hunga Ha’apai Eruption of 15 January 2022, *Geophysical Research Letters*, 49, e2022GL098131, <https://doi.org/https://doi.org/10.1029/2022GL098131>, e2022GL098131 2022GL098131, 2022.
- Dempsey, S. M., Hindley, N. P., Moffat-Griffin, T., Wright, C. J., Smith, A. K., Du, J., and Mitchell, N. J.: Winds and tides of the Antarctic mesosphere and lower thermosphere: One year of meteor-radar observations over Rothera (68°S, 68°W) and comparisons with WACCM and eCMAM, *Journal of Atmospheric and Solar-Terrestrial Physics*, 212, 105–110, <https://doi.org/https://doi.org/10.1016/j.jastp.2020.105510>, 2021.
- 355 Fritts, D. C., Janches, D., Imura, H., Hocking, W. K., Mitchell, N. J., Stockwell, R. G., Fuller, B., Vandeppeer, B., Hormaechea, J., Brunini, C., and Levato, H.: Southern Argentina Agile Meteor Radar: System design and initial measurements of large-scale winds and tides, *Journal of Geophysical Research: Atmospheres*, 115, <https://doi.org/10.1029/2010JD013850>, 2010.
- 360 Gudadze, N., Stober, G., and Chau, J. L.: Can VHF radars at polar latitudes measure mean vertical winds in the presence of PMSE?, *Atmospheric Chemistry and Physics*, 19, 4485–4497, <https://doi.org/10.5194/acp-19-4485-2019>, 2019.
- Hall, C. and Tsutsumi, M.: Neutral temperatures at 90 km altitude over Svalbard (78°N 16°E), 2002–2019, derived from meteor radar observations, *Polar Science*, 24, 100–110, <https://doi.org/https://doi.org/10.1016/j.polar.2020.100530>, 2020.
- 365 Hall, C. M. and Tsutsumi, M.: Changes in mesospheric dynamics at 78°N, 16°E and 70°N, 19°E: 2001–2012, *Journal of Geophysical Research: Atmospheres*, 118, 2689 – 2701, 2013.
- Heki, K.: Ionospheric signatures of repeated passages of atmospheric waves by the 2022 Jan. 15 Hunga Tonga-Hunga Ha’apai eruption detected by QZSS-TEC observations in Japan, *Earth, Planets and Space*, 74, <https://doi.org/10.1186/s40623-022-01674-7>, 2022.
- Hocking, W., Fuller, B., and Vandeppeer, B.: Real-time determination of meteor-related parameters utilizing modern digital technology, *Journal of Atmospheric and Solar-Terrestrial Physics*, 63, 155 – 169, [https://doi.org/http://dx.doi.org/10.1016/S1364-6826\(00\)00138-3](https://doi.org/http://dx.doi.org/10.1016/S1364-6826(00)00138-3), radar applications for atmosphere and ionosphere research - PIERS 1999, 2001.
- 370 Hocking, W. K., Thayaparan, T., and Jones, J.: Meteor decay times and their use in determining a diagnostic mesospheric Temperature-pressure parameter: Methodology and one year of data, *Geophysical Research Letters*, 24, 2977–2980, <https://doi.org/10.1029/97GL03048>, 1997.
- 375 Holdsworth, D. A., Reid, I. M., and Cervera, M. A.: Buckland Park all-sky interferometric meteor radar, *Radio Science*, 39, n/a–n/a, <https://doi.org/10.1029/2003RS003014>, rS5009, 2004.



- Imura, H., Fritts, D. C., Lieberman, R. S., Janches, D., Mitchell, N. J., Franke, S. J., Singer, W., Hocking, W. K., Taylor, M. J., and Moffat-Griffin, T.: Climatology of quasi-2-day wave structure and variability at middle latitudes in the northern and southern hemispheres, *Journal of Atmospheric and Solar-Terrestrial Physics*, 221, 105 690, <https://doi.org/https://doi.org/10.1016/j.jastp.2021.105690>, 2021.
- 380 Jacobi, C., Fröhlich, K., Viehweg, C., Stober, G., and Kürschner, D.: Midlatitude mesosphere/lower thermosphere meridional winds and temperatures measured with meteor radar, *Advances in Space Research*, 39, 1278–1283, <https://doi.org/https://doi.org/10.1016/j.asr.2007.01.003>, 2007.
- Liu, H.-L., Wang, W., Huba, J. D., Lauritzen, P. H., and Vitt, F.: Atmospheric and Ionospheric Responses to Hunga-Tonga Volcano Eruption Simulated by WACCM-X, *Geophysical Research Letters*, 50, e2023GL103 682, <https://doi.org/https://doi.org/10.1029/2023GL103682>,
385 e2023GL103682 2023GL103682, 2023.
- Marino, J., Palo, S. E., and Rainville, N.: First Observations From a New Meteor Radar at McMurdo Station Antarctica (77.8°S, 166.7°E), *Radio Science*, 57, e2022RS007 466, <https://doi.org/https://doi.org/10.1029/2022RS007466>, e2022RS007466 2022RS007466, 2022.
- Matoza, R. S., Fee, D., Assink, J. D., Iezzi, A. M., Green, D. N., Kim, K., Toney, L., Lecocq, T., Krishnamoorthy, S., Lalande, J.-M., Nishida, K., Gee, K. L., Haney, M. M., Ortiz, H. D., Brissaud, Q., Martire, L., Rolland, L., Vergados, P., Nippres, A., Park, J., Shani-Kadmiel, S.,
390 Witsil, A., Arrowsmith, S., Caudron, C., Watada, S., Perttu, A. B., Taisne, B., Mialle, P., Pichon, A. L., Vergoz, J., Hupe, P., Blom, P. S., Waxler, R., Angelis, S. D., Snively, J. B., Ringler, A. T., Anthony, R. E., Jolly, A. D., Kilgour, G., Averbuch, G., Ripepe, M., Ichihara, M., Arciniega-Ceballos, A., Astafyeva, E., Ceranna, L., Cevuard, S., Che, I.-Y., Negri, R. D., Ebeling, C. W., Evers, L. G., Franco-Marin, L. E., Gabrielson, T. B., Hafner, K., Harrison, R. G., Komjathy, A., Lacanna, G., Lyons, J., Macpherson, K. A., Marchetti, E., McKee, K. F., Mellors, R. J., Mendo-Pérez, G., Mikesell, T. D., Munaibari, E., Oyola-Merced, M., Park, I., Pilger, C., Ramos, C., Ruiz, M. C., Sabatini,
395 R., Schwaiger, H. F., Tailpied, D., Talmadge, C., Vidot, J., Webster, J., and Wilson, D. C.: Atmospheric waves and global seismoacoustic observations of the January 2022 Hunga eruption, *Tonga, Science*, 377, 95–100, <https://doi.org/10.1126/science.abo7063>, 2022.
- Meek, C. E., Manson, A. H., Hocking, W. K., and Drummond, J. R.: Eureka, 80°N, SKiYMET meteor radar temperatures compared with Aura MLS values, *Annales Geophysicae*, 31, 1267–1277, <https://doi.org/10.5194/angeo-31-1267-2013>, 2013.
- Millán, L., Santee, M. L., Lambert, A., Livesey, N. J., Werner, F., Schwartz, M. J., Pumphrey, H. C., Manney, G. L., Wang, Y., Su, H., Wu,
400 L., Read, W. G., and Froidevaux, L.: The Hunga Tonga-Hunga Ha’apai Hydration of the Stratosphere, *Geophysical Research Letters*, 49, e2022GL099 381, <https://doi.org/https://doi.org/10.1029/2022GL099381>, e2022GL099381 2022GL099381, 2022.
- Miyoshi, Y. and Shinagawa, H.: Upward propagation of gravity waves and ionospheric perturbations triggered by the 2022 Hunga-Tonga volcanic eruption, *Earth Planets Space*, 75, <https://doi.org/doi.org/10.1186/s40623-023-01827-2>, 2023.
- National Imagery and Mapping Agency: Department of Defense World Geodetic System 1984: its definition and relationships with local
405 geodetic systems, Tech. Rep. TR8350.2, National Imagery and Mapping Agency, St. Louis, MO, USA, http://earth-info.nga.mil/GandG/publications/tr8350.2/tr8350_2.html, 2000.
- Nozawa, S., Imaida, S., Brekke, A., Hall, C. M., Manson, A., Meek, C., Oyama, S., Dobashi, K., and Fujii, R.: The quasi 2-day wave observed in the polar mesosphere, *Journal of Geophysical Research: Atmospheres*, 108, ACL 3–1–ACL 3–12, <https://doi.org/https://doi.org/10.1029/2002JD002440>, 2003.
- 410 Poblet, F. L., Chau, J. L., Conte, J. F., Vierinen, J., Suclupe, J., Liu, A., and Rodriguez, R. R.: Extreme Horizontal Wind Perturbations in the Mesosphere and Lower Thermosphere Over South America Associated With the 2022 Hunga Eruption, *Geophysical Research Letters*, 50, e2023GL103 809, <https://doi.org/https://doi.org/10.1029/2023GL103809>, e2023GL103809 2023GL103809, 2023.
- Pokhotelov, D., Becker, E., Stober, G., and Chau, J. L.: Seasonal variability of atmospheric tides in the mesosphere and lower thermosphere: meteor radar data and simulations, *Annales Geophysicae*, 36, 825–830, <https://doi.org/10.5194/angeo-36-825-2018>, 2018.



- 415 Shinbori, A., Otsuka, Y., Sori, T., Nishioka, M., Perwitasari, S., Tsuda, T., and Nishitani, N.: Electromagnetic conjugacy of ionospheric disturbances after the 2022 Hunga Tonga-Hunga Ha'apai volcanic eruption as seen in GNSS-TEC and SuperDARN Hokkaido pair of radars, *Earth, Planets and Space*, 74, <https://doi.org/10.1186/s40623-022-01665-8>, 2022.
- Stober, G., Baumgarten, K., McCormack, J. P., Brown, P., and Czarnecki, J.: Comparative study between ground-based observations and NAVGEM-HA analysis data in the mesosphere and lower thermosphere region, *Atmospheric Chemistry and Physics*, 20, 11 979–12 010, <https://doi.org/10.5194/acp-20-11979-2020>, 2020.
- 420 Stober, G., Janches, D., Matthias, V., Fritts, D., Marino, J., Moffat-Griffin, T., Baumgarten, K., Lee, W., Murphy, D., Kim, Y. H., Mitchell, N., and Palo, S.: Seasonal evolution of winds, atmospheric tides, and Reynolds stress components in the Southern Hemisphere mesosphere–lower thermosphere in 2019, *Annales Geophysicae*, 39, 1–29, <https://doi.org/10.5194/angeo-39-1-2021>, 2021a.
- Stober, G., Kozlovsky, A., Liu, A., Qiao, Z., Tsutsumi, M., Hall, C., Nozawa, S., Lester, M., Belova, E., Kero, J., Espy, P. J., Hibbins, R. E.,
425 and Mitchell, N.: Atmospheric tomography using the Nordic Meteor Radar Cluster and Chilean Observation Network De Meteor Radars: network details and 3D-Var retrieval, *Atmospheric Measurement Techniques*, 14, 6509–6532, <https://doi.org/10.5194/amt-14-6509-2021>, 2021b.
- Stober, G., Kuchar, A., Pokhotelov, D., Liu, H., Liu, H.-L., Schmidt, H., Jacobi, C., Baumgarten, K., Brown, P., Janches, D., Murphy, D., Kozlovsky, A., Lester, M., Belova, E., Kero, J., and Mitchell, N.: Interhemispheric differences of mesosphere–lower thermosphere winds
430 and tides investigated from three whole-atmosphere models and meteor radar observations, *Atmospheric Chemistry and Physics*, 21, 13 855–13 902, <https://doi.org/10.5194/acp-21-13855-2021>, 2021c.
- Stober, G., Liu, A., Kozlovsky, A., Qiao, Z., Kuchar, A., Jacobi, C., Meek, C., Janches, D., Liu, G., Tsutsumi, M., Gulbrandsen, N., Nozawa, S., Lester, M., Belova, E., Kero, J., and Mitchell, N.: Meteor radar vertical wind observation biases and mathematical debiasing strategies including the 3DVAR+DIV algorithm, *Atmospheric Measurement Techniques*, 15, 5769–5792, <https://doi.org/10.5194/amt-15-5769-2022>, 2022.
- 435 Stober, G., Liu, A., Kozlovsky, A., Qiao, Z., Krochin, W., Shi, G., Kero, J., Tsutsumi, M., Gulbrandsen, N., Nozawa, S., Lester, M., Baumgarten, K., Belova, E., and Mitchell, N.: Identifying gravity waves launched by the Hunga Tonga–Hunga Ha'apai volcanic eruption in mesosphere/lower-thermosphere winds derived from CONDOR and the Nordic Meteor Radar Cluster, *Annales Geophysicae*, 41, 197–208, <https://doi.org/10.5194/angeo-41-197-2023>, 2023.
- 440 Themens, D. R., Watson, C., Žagar, N., Vasylyevych, S., Elvidge, S., McCaffrey, A., Prikryl, P., Reid, B., Wood, A., and Jayachandran, P. T.: Global Propagation of Ionospheric Disturbances Associated With the 2022 Tonga Volcanic Eruption, *Geophysical Research Letters*, 49, e2022GL098 158, <https://doi.org/https://doi.org/10.1029/2022GL098158>, e2022GL098158 2022GL098158, 2022.
- Vadas, S. L. and Azeem, I.: Concentric Secondary Gravity Waves in the Thermosphere and Ionosphere Over the Continental United States on March 25–26, 2015 From Deep Convection, *Journal of Geophysical Research: Space Physics*, 126, e2020JA028 275, <https://doi.org/https://doi.org/10.1029/2020JA028275>, e2020JA028275 2020JA028275, 2021.
- 445 Vadas, S. L. and Becker, E.: Numerical Modeling of the Excitation, Propagation, and Dissipation of Primary and Secondary Gravity Waves during Wintertime at McMurdo Station in the Antarctic, *Journal of Geophysical Research: Atmospheres*, 123, 9326–9369, <https://doi.org/10.1029/2017JD027974>, 2018.
- Vadas, S. L., Fritts, D. C., and Alexander, M. J.: Mechanism for the Generation of Secondary Waves in Wave Breaking Regions, *Journal of the Atmospheric Sciences*, 60, 194 – 214, [https://doi.org/https://doi.org/10.1175/1520-0469\(2003\)060<0194:MFTGOS>2.0.CO;2](https://doi.org/https://doi.org/10.1175/1520-0469(2003)060<0194:MFTGOS>2.0.CO;2), 2003.
- 450



- Vadas, S. L., Makela, J. J., Nicolls, M. J., and Milliff, R. F.: Excitation of gravity waves by ocean surface wave packets: Upward propagation and reconstruction of the thermospheric gravity wave field, *Journal of Geophysical Research: Space Physics*, 120, 9748–9780, <https://doi.org/https://doi.org/10.1002/2015JA021430>, 2015.
- 455 Vadas, S. L., Becker, E., Figueiredo, C., Bossert, K., Harding, B. J., and Gasque, L. C.: Primary and Secondary Gravity Waves and Large Scale Wind Changes Generated by the Tonga Volcanic Eruption on 15 January 2022: Modeling and Comparison With ICON-MIGHTI Winds, *Journal of Geophysical Research: Space Physics*, 128, e2022JA031138, <https://doi.org/https://doi.org/10.1029/2022JA031138>, e2022JA031138 2022JA031138, 2023a.
- Vadas, S. L., Figueiredo, C., Becker, E., Huba, J. D., Themens, D. R., Hindley, N. P., Mrak, S., Galkin, I., and Bossert, K.: Traveling ionospheric disturbances induced by the secondary gravity waves from the Tonga eruption on 15 January 2022: Modeling with MESO-460 RAC/HIAMCM/SAMI3 and comparison with GPS/TEC and ionosonde data, *Journal of Geophysical Research: Space Physics*, n/a, e2023JA031408, <https://doi.org/https://doi.org/10.1029/2023JA031408>, e2023JA031408 2023JA031408, 2023b.
- Webster, A. R., Brown, P. G., Jones, J., Ellis, K. J., and Campbell-Brown, M.: Canadian Meteor Orbit Radar (CMOR), *Atmospheric Chemistry and Physics*, 4, 679–684, <https://doi.org/10.5194/acp-4-679-2004>, 2004.
- 465 Wright, C. J., Hindley, N. P., Alexander, M. J., Barlow, M., Hoffmann, L., Mitchell, C. N., Prata, F., Bouillon, M. and Carstens, J., Clerbaux, C., Osprey, S. M., Powell, N., Randall, C. E., and Yue, J.: Surface-to-space atmospheric waves from Hunga Tonga-Hunga Ha’apai eruption, *Nature*, 609, 741–746, <https://doi.org/https://doi.org/10.1038/s41586-022-05012-5>, 2022.
- Yamada, M., Ho, T.-C., Mori, J., Nishikawa, Y., and Yamamoto, M.-Y.: Tsunami Triggered by the Lamb Wave From the 2022 Tonga Volcanic Eruption and Transition in the Offshore Japan Region, *Geophysical Research Letters*, 49, e2022GL098752, <https://doi.org/https://doi.org/10.1029/2022GL098752>, e2022GL098752 2022GL098752, 2022.
- 470 Yang, C., Lai, D., Yi, W., Wu, J., Xue, X., Li, T., Chen, T., and Dou, X.: Observed Quasi 16-Day Wave by Meteor Radar over 9 Years at Mengcheng (33.4° N, 116.5°E) and Comparison with the Whole Atmosphere Community Climate Model Simulation, *Remote Sensing*, 15, <https://doi.org/10.3390/rs15030830>, 2023.
- Zeng, J., Yi, W., Xue, X., Reid, I., Hao, X., Li, N., Chen, J., Chen, T., and Dou, X.: Comparison between the Mesospheric Winds Observed by Two Collocated Meteor Radars at Low Latitudes, *Remote Sensing*, 14, <https://doi.org/10.3390/rs14102354>, 2022.
- 475 Zhang, S.-R., Vierinen, J., Aa, E., Goncharenko, L. P., Erickson, P. J., Rideout, W., Coster, A. J., and Spicher, A.: 2022 Tonga volcanic eruption induced global propagation of ionospheric disturbances via Lamb waves, 2022.